Nanoscale

Accepted Manuscript

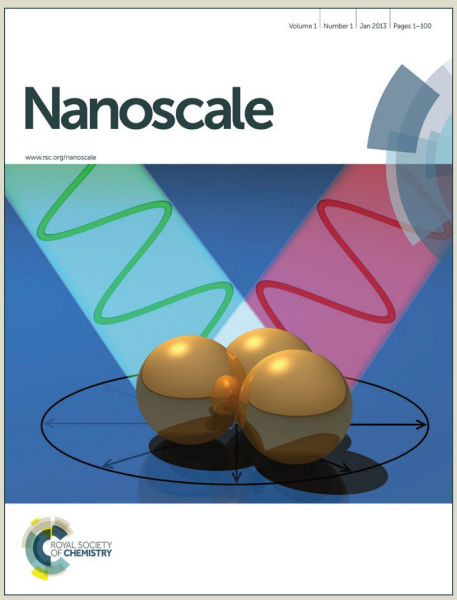

ROYAL SOCIETY OF CHEMISTRY

www.rsc.org/nanoscale

Journal Name

ARTICLE

Novel mesoporous P-doped graphitic carbon nitride nanosheets coupled with $ZnIn_2S_4$ nanosheets as efficient visible light driven heterostructures with remarkable enhanced photo-reduction activity

Received 00th January 20xx,
Accepted 00th January 20xx

DOI: 10.1039/x0xx00000x

www.rsc.org/

Wei Chen, Tian-Yu Liu, Ting Huang, Xiao-Heng Liu* and Xu-Jie Yang

In this report, we rationally designed and fabricated the P-C_3N_4/$ZnIn_2S_4$ nanocomposites by in- situ immobilizing $ZnIn_2S_4$ nanosheets on the surface of mesoporous P-doped graphite carbon nitrogen (P-C_3N_4) nanosheets at the mixed solvothermal environment and the application for the photoreduction of 4-nitroaniline was used to estimate their photocatalytic performance. Different with template route, here the mesoporous P-C_3N_4 nanosheets was prepared with template-free strategy. The as-fabricated P-C_3N_4/$ZnIn_2S_4$ nanocomposites were systematically characterized by analyzing the phase structure, chemical components, electronic and optical properties and separation of charge carrier pairs. More importantly, these P-C_3N_4/$ZnIn_2S_4$ heterostructures have been proved to be highly efficient visible light responsive photocatalysts for photo-reduction and meanwhile exhibits excellent photo-stability during the recycling runs. The sufficient evidences reveal that the significantly improved photocatalytic performance is mainly attributed to the more efficient charge carrier separation based on the construction of close heterogeneous interface. This work may provide new insights into utilizing P-C_3N_4/$ZnIn_2S_4$ nanocomposites as visible light driven photocatalysts for group conversion in the field of fine chemical engineering.

1. Introduction

Recent decades, semiconductor materials have been undergoing fast development because of their intrinsically fascinating properties and potentially promising applications in a wide of fields, such as catalysts,[1,2] electron devices,[3,4] and bioimaging.[5] Among them, photocatalytic applications have been emerged as a new technology for pollution abatement, energy production and organic catalytic reaction since Fujishima and Honda found that TiO_2 electrode can be utilized for photoelectrochemical water splitting for hydrogen evolution in 1972.[6] However, the major drawback of most of metal oxide photocatalysts is the large band gap corresponding to just effective response in ultraviolet light region, which only accounts for 4% of total sunlight spectrum reaching to the surface of earth. As such, some nanostructured metal sulfide semiconductors have been prepared and used for photocatalysis in visible light range due to the small band gap. Ternary chalcogenide $ZnIn_2S_4$, as a typical member of sulfide semiconductor, is endowed with the features of visible light harvesting benefitted from narrow band gap and extensive applications resulted from appropriate band edges.[7, 8] Besides, the $ZnIn_2S_4$ also exhibits considerable stability during the photocatalytic process. Despite $ZnIn_2S_4$ possesses these advantages, the photocatalytic activity and photo-stability still need to improve for propose of industrial applications. Many researches reveal that sulfide based nanocomposite materials is an important means to enhance its activity and strengthen photo resistance. Zhou et al. [9] fabricated RGO-$ZnIn_2S_4$ nanocomposites via the in situ growth solvothermal process. These nanocomposite show excellent H_2 production at rate of 1632 $mmol \cdot g^{-1} \cdot h^{-1}$ without the presence of expensive Pt as a cocatalyst and photocatalytic activity almost does not present an attenuation after light irradiation for 12h. Gao et al. [10] reported the fabrication of Fe_2O_3-$ZnIn_2S_4$ and FeOOH-$ZnIn_2S_4$ nanocomposites with enhanced degradation efficiency of 2,4,6-TBP comparing with $ZnIn_2S_4$ both under UV and visible light illumination. Based on above results, we hold the view that $ZnIn_2S_4$ based nanocomposites may be perfect photocatalysts for photocatalytic practice.

Metal-free graphitic carbon nitrogen (g-C_3N_4), has attracted intensive interest as a visible light responsive photocatalyst due to low cost, simple synthesis, good photo-stability and appropriate band gap and band potentials. These features endow it as a promising candidate to achieve energy conversion from solar energy to chemical energy. However, the pure g-C_3N_4 with bulk structure often exhibits low photocatalytic efficiency with the quantum yield only about 0.1% at 420-460 nm as a result of the formation of grain boundary defects under high-temperature condition, which would create many grain boundary defects leading to faster recombination of charge carrier pairs.[11, 12] Although many

Key Laboratory of Education Ministry for Soft Chemistry and Functional Materials, Nanjing University of Science and Technology, Nanjing 210094, China
E-mail: xhliu@mail.njust.edu.cn(X.H. Liu);
Electronic Supplementary Information (ESI) available: [details of any supplementary information available should be included here]. See DOI: 10.1039/x0xx00000x

strategies, including morphology modulation,[13,14] surface functionalization,[15,16] thickness control, [17,18]electronic state regulation[19-21] and mesoporous development,[11,22] have been devoted to improving the photocatalytic efficiency. Unsatisfactorily, the photocatalytic activity of g-C_3N_4 is still too low to meet the requirements for extensive practical applications. Therefore, some synergetic tactics were applied to further optimize the catalytic performance, such as the construction of porous ultrathin nanosheets, the development of functional nanosheets and the preparation of doping porous network, etc.[23-25] Mesoporous g-C_3N_4 ultrathin nanosheets have attracted tremendous attention from researchers based on their characters of enhanced light harvesting, shorter diffusion distance of charge carriers pairs and reduced interior defects. Besides, these ultrathin structures with pore also provides perfect platform as two-dimensional catalyst support. Recently, some attempts have been made by our group via coupling porous g-C_3N_4 ultrathin nanosheets with other semiconductors photocatalysts to possess more highly efficient photocatalytic activities.[18] These nanocomposites exhibits significantly enhanced photocatalytic performance for pollutants removal and hydrogen generation from water splitting; meanwhile the photo-stability could also be strengthened because of the introduction of porous g-C_3N_4 ultrathin nanosheets. It was reported that phosphorus doped g-C_3N_4 (P-C_3N_4) would promote the separation of photogenerated hole and electron pairs, thus benefiting the photocatalytic activity. [26, 27] To our knowledge, the architecture combining mesoporous ultrathin structure and P-doped into g-C_3N_4 has not been published. Here, we prepared the mesoporous P-C_3N_4 ultrathin nanosheets by frozen expansion and post-thermal exfoliation strategy. In fact, these mesoporous P-C_3N_4 ultrathin nanosheets material exhibits superior visible light responsive catalytic activity to bulk P-C_3N_4 and porous g-C_3N_4 ultrathin nanosheets.

Inspired by above investigations, we firstly designed and synthesized the P-C_3N_4/$ZnIn_2S_4$ with close 2D-2D heterogeneous interface by mixed solvothermal route and evaluated their photocatalytic performance from the conversion of nitro group. The fabrication processes involve the preparation and exfoliation of bulk P-C_3N_4 and in-situ immobilizing of $ZnIn_2S_4$ onto the surface of P-C_3N_4 nanosheets. We anticipate this binary architecture would integrate the above-mentioned merits of $ZnIn_2S_4$ nanosheets and mesoporous P-C_3N_4 ultrathin nanosheets collectively.

2. Experimental

2.1 Materials

Melamine ($C_6H_6N_6$, AR), zinc nitrate hexahydrate ($Zn(NO_3)_2.6H_2O$, AR) and L-cysteine (Cys, AR) were purchased from Sinopharm Chemical Reagent Co., Ltd. (Shanghai, China). Hexachlorotriphosphazene ($Cl_6N_3P_3$, 98%) was provided by Sigma-Aldrich. Indium chloride ($InCl_3$, 98%) and ammonium formate (CH_5NO_2, AR) were obtained from Aladdin. All reagents were used without further purification.

2.2 Preparation

Bulk P-doped g-C_3N_4 (P-C_3N_4), the precursor of mesoporous P-C_3N_4 ultrathin nanosheets in this work, was prepared by thermal polycondensation of mixture including 90 wt% of melamine and 10 wt% of hexachlorotriphosphazene at heating rate of 2.3 $K{\cdot}min^{-1}$ to reach 550 ^{o}C and keep at this temperature for another 4 hours in air. The mesoporous P-C_3N_4 ultrathin nanosheets were synthesized by frozen expansion and post-thermal exfoliation from bulk P-C_3N_4 according to the reports in our previous studies. [18, 23]The fabrication of P-C_3N_4/$ZnIn_2S_4$ nanocomposites with different weight addition ratios of P-C_3N_4 ultrathin nanosheets was typically performed as follows. Mesoporous P-C_3N_4 ultrathin nanosheets were dispersed completely into mixed solvent consisting of 40 mL of deionized water and 20 mL of absolute ethanol by ultrasonication, then zinc nitrate hexahydrate (1 mmol, 0.297g) and Indium chloride (2 mmol, 0.452g) were dissolved into above suspension, and the mixture was stirred magnetically for 2 hours. During this process, the positively charged Zn^{2+} and In^{3+} can be adsorbed onto the surface of P-C_3N_4 ultrathin nanosheets with negative charge by the electrostatic attraction. Subsequently, 4mmoL (0.485g) of L-cysteine, employed as the source of sulphur, was quickly added and kept further stirring for 4 hours. Then, the mixture was transferred to a 100 mL of polytetrafluoroethylene-lined stainless autoclave at 453 K for 12 hours under autogenous pressure in an electric oven, which allows the formation of $ZnIn_2S_4$ nanosheets on the P-C_3N_4 ultrathin platform. After cooling down to room temperature naturally, the products was collected, washed by water, and fully dried at 333 K to obtain the final P-C_3N_4/$ZnIn_2S_4$ nanocomposites with different weight addition ratios of P-C_3N_4 to $ZnIn_2S_4$ sample, namely, 5, 10, 20 and 30 wt% P-C_3N_4/$ZnIn_2S_4$ nanocomposites. For comparison, bare $ZnIn_2S_4$ was prepared using the same procedures without the addition of P-C_3N_4.

2.2 Characterization

The crystalline phases of P-C_3N_4/$ZnIn_2S_4$ was analyzed by Bruker D8 Advance diffractometer with Cu Kα radiation (λ=0.15418 nm) in the range of 2θ =10- 60 ^{o}. Sample morphology and microstructure were separately observed by scanning electron microscope (TM3030, Hitachi) and transmission electron microscope (TEM, Tecnai G2 F20 S-TWIN). Fourier transform infrared (FT-IR) spectra were measured by a Nicolet IS10 infrared spectrometer. The optical properties of the samples were measured using UV-vis diffuse reflectance spectroscopy (Hitachi, UV-365) with $BaSO_4$ as the reflectance standard. The specific surface areas were measured using the on a BET instrument and the pore diameter distribution was obtained from the absorption isotherms of N_2 using the Barrett-Joyner-Halenda (BJH) equation (JW-BK132F, JWGB SCI&TECH, China). The surface composition analysis and electronic binding energy of samples were acquired by a Thermo ESCALAB 250Xi X-ray photoelectron spectrometer under an Al Kα radiation (hv = 1486.6 eV). Solid-state fluorescence measurements (λ_{ex} = 363 nm) were recorded from 350 to 700 nm on a JASCO FP-6500 type fluorescence spectrophotometer using 1 nm slit width. The photoelectrodes of samples were prepared to investigate the transition of photogenerated electrons and the photoelectrochemical properties were measured on a CHI-660E electrochemical workstation (Shanghai Chenhua Instrument Co., Ltd, China) in a standard three-electrode system using the prepared samples with an active area of ca. 0.5 cm × 0.5 cm as the working

electrodes, a platinum wire as the counter electrode, and Ag/AgCl as the reference electrode and Na_2SO_4 (0.1 M) aqueous solution was used as the electrolyte. Electrochemical impedance spectra (EIS) were recorded at the open circuit potential by applying an AC voltage with 5 mV amplitude.

2.3 Photocatalytic tests

The photocatalytic activities of as-prepared samples were evaluated by photoredox reactions of 4-nitroaniline (4-NA) under visible light irradiation (λ > 400 nm). Visible light irradiation was obtained from a Xenon lamp (XL-300, Yirda). Typically, 30 mg of photocatalysts and 90 mg of ammonium formate were completely added into 30 mL of 4-NA solution with initial concentration of 10 $mg{\cdot}L^{-1}$. Prior to irradiation, the suspension was drastically stirred in the dark for 2h to achieve adsorption-desorption equilibrium between the photocatalysts and 4-NA. At an interval of 15 minutes, 3 mL aliquots were collected, centrifuged, and then the solution was analyzed on a UV-vis spectrometer (UV-1801). The whole experimental process was conducted in a flowing-nitrogen atmosphere at a flow rate of 100 $mL{\cdot}min^{-1}$.

3. Results and discussion

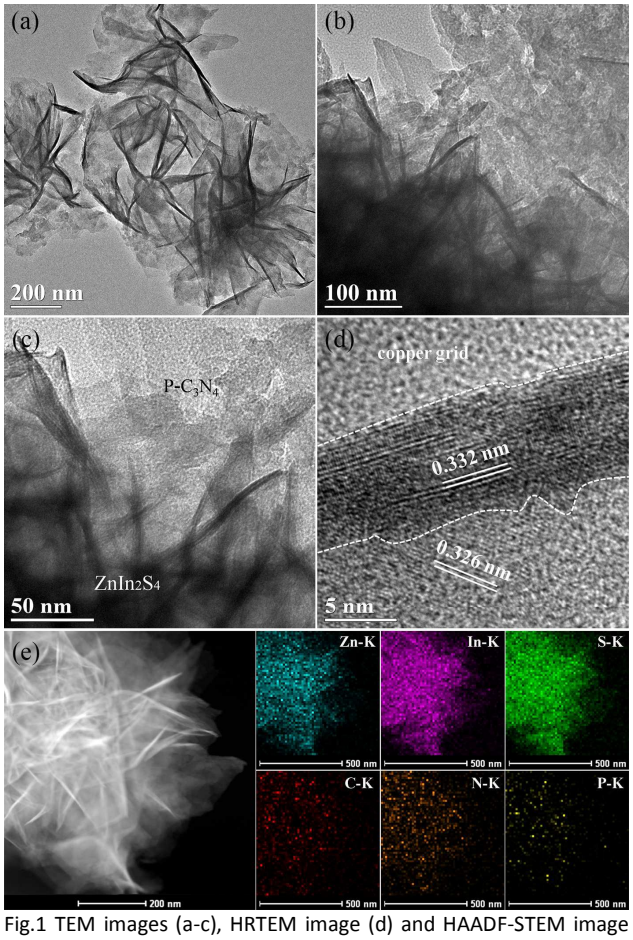

Fig.1 TEM images (a-c), HRTEM image (d) and HAADF-STEM image of 20 wt% P-C_3N_4/$ZnIn_2S_4$ nanocomposites.

The morphology and microstructure of synthesized samples were analyzed by TEM and SEM observations. Fig.1 (a-c) show the TEM images of 20 wt% P-C_3N_4/$ZnIn_2S_4$ nanocomposites, from which we can find that $ZnIn_2S_4$ nanosheets were close immobilized onto the surface P-C_3N_4 nanosheets via 2D-2D heterojunction interface. Clear lattice spacing of 0.322 nm and 0.326 nm can be assigned to the (102) crystal plane of $ZnIn_2S_4$ nanosheets with hexagonal phase and (002) plane of P-C_3N_4 nanosheets as evidenced provided from Fig. 1d. The results from high-angle annular dark-field scanning transmission electron microscopy (HAADF-STEM) images and corresponding to elemental mapping indicate that definite coexistence of P-C_3N_4 and $ZnIn_2S_4$ in the heterostructures. This result gives solid evidence that $ZnIn_2S_4$ nanosheets are successfully immobilized onto the surface of P-C_3N_4 nanosheets. The pure P-C_3N_4 sample displays loose and wrinkled lamellar-like structure with porous feature as depicted in Fig. S1a. Amounts of sphere-like structures composed of two-dimensional nanoflakes are presented in 20 wt% P-C_3N_4/$ZnIn_2S_4$ nanocomposites, which are wrapped by P-C_3N_4 nanosheets (Fig. S1b). The EDX elemental mapping was employed to determine the elementary composition and dispersion of $ZnIn_2S_4$ in the hybrid sample. As can be seen from Fig. S1(d,e), it is obvious that 20 wt% P-C_3N_4/$ZnIn_2S_4$ architectures was composed of Zn, In, S, P, C and N elements, further revealing the formation of $ZnIn_2S_4$ in the presence of P-C_3N_4 nanosheets. Besides, this nanocomposite implies the uniform distribution of $ZnIn_2S_4$ on P-C_3N_4 nanosheets.

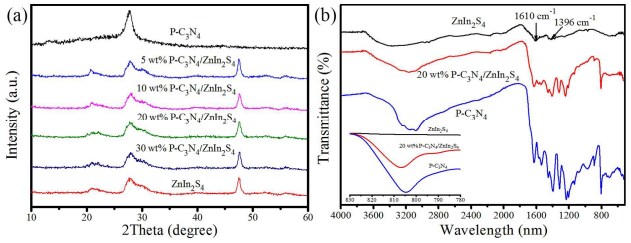

Fig.2 Typical XRD patterns (a) and FT-IR spectra (b) of pure P-C_3N_4, bare $ZnIn_2S_4$ as well as P-C_3N_4/$ZnIn_2S_4$ nanocomposites.

Typical X-ray diffraction (XRD) patterns of the as-fabricated P-C_3N_4/$ZnIn_2S_4$ nanocomposites with different P-C_3N_4 content are shown in Fig. 2a. The characteristic peak of pure P-C_3N_4 ultrathin nanosheets around 27.7° could be clearly identified as (002) diffraction plane, which is resulted from the inter-planar stacking peak of aromatic systems.[28] And the weak diffraction peak at 13.0 °, representing the in-plane structural packing motif, could be perfectly index to (100) diffraction plane for graphitic materials.[29] Moreover, all diffraction peaks of $ZnIn_2S_4$ nanosheets are in well accordance with the hexagonal $ZnIn_2S_4$ phase as evidenced from the PXRD patterns (JCPDS: 65-2023).[30] The P-C_3N_4/$ZnIn_2S_4$ nanocomposites shows similar XRD pattern with pure hexagonal $ZnIn_2S_4$ sample, indicating that the introduction of P-C_3N_4 nanosheets in the reaction does not influence the formation of hexagonal $ZnIn_2S_4$. The reasons why no typical diffraction peaks ascribed to the P-C_3N_4 nanosheets in P-C_3N_4/$ZnIn_2S_4$ hybrid samples are presented could be concluded as follows: (i) the (100) reflections of P-C_3N_4 are not observed in P-C_3N_4/$ZnIn_2S_4$ nanocomposite because the regular stack of P-C_3N_4 was destroyed by the intercalation of $ZnIn_2S_4$ nanosheets; (ii) no (002) diffraction peak of P-C_3N_4 in the XRD pattern of nanocomposite is presented,

which is probably due to diffraction overlap between P-C_3N_4 (002) and $ZnIn_2S_4$ (102) planes. However, the existence of P-C_3N_4 nanosheets in the nanocomposite can be confirmed by the Fourier transform infrared (FT-IR) spectra. As observed in Fig.2b, the FT-IR spectrum of pure P-C_3N_4 nanosheets reveals that s-triazine ring unit breathing vibration is at 805 cm^{-1}.[26] And a series of peaks of P-C_3N_4 nanosheets located between 1200 cm^{-1} and 1650cm^{-1} with the characteristic peaks at 1233, 1316, 1396, and 1627 cm^{-1} belongs to the typical stretching vibration of C=N and C-N heterocycles.[31] These peaks were slight blue-shift in comparison to the values of g-C_3N_4 in previous reports, indicating the doping of P into g-C_3N_4 lattice. Additionally, the broad band located at 3000-3500 cm^{-1} is attributable to stretching vibration of surface adsorbed H_2O, primary amines (-NH_2) attached to the sp^2 hybridized carbon and secondary (=NH) amines located at the defect sites of the aromatic ring. For the $ZnIn_2S_4$ sample, two peaks at about 1610 cm^{-1} and 1396 cm^{-1} is due to the physically absorbed water molecules and hydroxyl groups. [32] After combination with P-C_3N_4, the FT-IR spectra of P-C_3N_4/$ZnIn_2S_4$ sample are similar to that of pure P-C_3N_4, except with weaker FT-IR mode. Such phenomena may be resulted from reduction of surface functional groups due to bonding reaction of P-C_3N_4 nanosheets with $ZnIn_2S_4$.[33] The fine scanned FT-IR spectra (inset, Fig.2b) of was employed to investigate the chemical interaction between P-C_3N_4 nanosheets and $ZnIn_2S_4$ nanosheets. Note that, after coupling, the s-triazine ring vibration of obtained 20 wt% P-C_3N_4/$ZnIn_2S_4$ exhibits obvious red-shift towards longer wavelength direction, which is an indicator of the presence of chemical interaction.

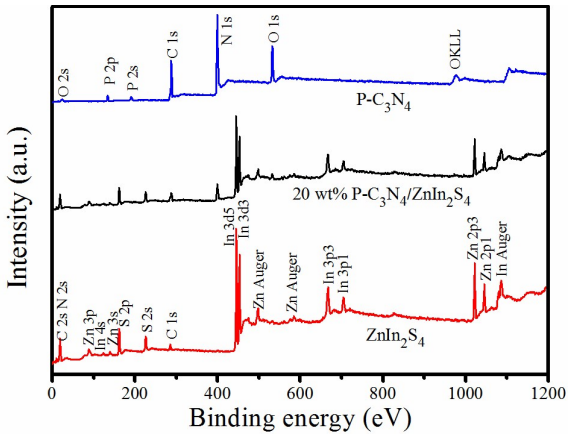

Fig.3 XPS survey spectra of the as-fabricated P-C_3N_4, $ZnIn_2S_4$ and 20 wt% P-C_3N_4/$ZnIn_2S_4$ nanocomposites.

The UV-Vis diffuse reflectance properties of P-C_3N_4/$ZnIn_2S_4$ nanocomposites with different P-C_3N_4 concentration were illustrated in Fig. S3. Clearly, the bare $ZnIn_2S_4$ sample exhibits strong solar light absorption from the UV region to the visible light range up to 450 nm, while the steep absorption edge of pure P-C_3N_4 nanosheets just locates at around 430 nm, smaller than that of g-C_3N_4 reported at 460 nm. Compared with the pristine $ZnIn_2S_4$, the obvious blue shift absorption in the wavelength range larger than 400 nm has been presented in P-C_3N_4/$ZnIn_2S_4$ hybrid samples, which may be attributed to the shield effect resulted from the covering of P-C_3N_4 on $ZnIn_2S_4$ surface. The subdued visible light absorption in the visible-light region is apparently detrimental for the generation of photo-induced charge carrier.

The surface elemental composites and electronic state of pure P-C_3N_4, original $ZnIn_2S_4$ as well as 20 wt% P-C_3N_4/$ZnIn_2S_4$ were investigated by X-ray photoelectron spectroscopy (XPS). Fig.3 exhibits the XPS survey spectra of these three different samples, from which, we can find that all signals assigned to Zn, In, S, C, N and P elements are detected in the survey XPS spectrum of the 20 wt% P-C_3N_4/$ZnIn_2S_4$ nanocomposites. This result further suggests that the hybrid sample is composed of P-C_3N_4 and $ZnIn_2S_4$. To in-depth investigate the interaction between P-C_3N_4 and $ZnIn_2S_4$ in P-C_3N_4/$ZnIn_2S_4$ nanocomposites, the high-resolution XPS were carried out and displayed in Fig.4. The C 1s spectra of P-C_3N_4-related samples have two obvious peaks at 284.8 and 288.4 eV for pure P-C_3N_4, 284.8 and 288.1 eV for 20 wt% P-C_3N_4/$ZnIn_2S_4$, corresponding to referred carbon and defect-containing sp^2-bonded carbon (-N=C-N) in graphitic carbon nitride, respectively.[5] The XPS spectrum of N 1s region from P-C_3N_4 can be deconvoluted into four smaller peaks with the binding energy of 398.8, 399.6, 401.4 and 404.8 eV. The main N 1s peak at 398.8 eV could be attributed to sp^2-hybridized nitrogen atom bonded to carbon atom (C=N-C), whereas the peak at 399.6 eV is related to either N-$(C)_3$ groups in connection with structural motif (C_6N_7) or amino groups ($(C)_2$–N–H) linking with structural defects and incomplete condensation. The weak peak located at 401.4 are due to the presence of N–$(C)_3$ group in the aromatic cycles resulted from nitrogen atoms bonded to three carbon atoms.[34] Besides, a negligible peak at 404.8 eV originates from π-excitations. The characteristic binding energies at 1021.8 and 1044.8 eV for Zn 2p, 444.9 and 445.2 eV for In 3d, 161.4 and 162.6 eV for S 2p are observed in alone $ZnIn_2S_4$.[35] Compared with $ZnIn_2S_4$, The binding energy of as-fabricated nanocomposites for Zn 2p region is not changed, nor are those of S 2p. However, after coupling with P-C_3N_4, the binding energies of C, N and In elements show a slight shift, which verifies the interaction between $ZnIn_2S_4$ nanosheets and P-C_3N_4 nanosheets. This result is in well accordance with the result of FT-IR. The interaction is further confirmed by binding energy variation of P 2p region just presented in Fig. 4f.

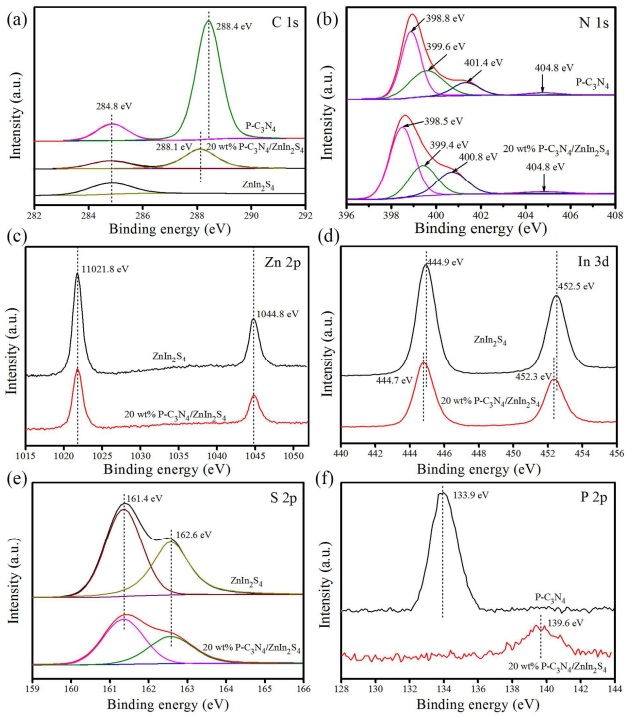

Fig.4 High resolution XPS spectra of the P-C_3N_4, $ZnIn_2S_4$ and 20 wt% P-C_3N_4/$ZnIn_2S_4$ nanocomposites at different regions: (a) C 1s, (b) N 1s, (c) Zn 2p, (d) In 3d, (e) S 2p and (f) P 2p.

Nitrogen adsorption-desorption isotherms (Fig. 5) were employed to characterize the specific surface areas and pore-size distribution of the P-C_3N_4, $ZnIn_2S_4$ as well as P-C_3N_4/$ZnIn_2S_4$ nanocomposites. The obtained results from sorption isotherms suggest that all samples exhibits a type IV isotherms with a H3 hysteresis loop, indicating the existence of mesoporous structure and (or) slit-like pore according to IUPAC standard.[36,37] The porous structure is further confirmed by pore-size distribution estimated by Barrett–Joyner–Halenda(BJH) method from the absorption branch of the isotherm. The BET surface area (S_{BET}) of the pure P-C_3N_4 and bare $ZnIn_2S_4$ was decided to be 30.6 and 57.2 $m^2 \cdot g^{-1}$, respectively, while that of 20 wt% nanocomposites was 50.3 $m^2 \cdot g^{-1}$, which is lower than that of $ZnIn_2S_4$.The reduction of S_{BET} in binary sample may be ascribed to the surface covering of P-C_3N_4 nanosheets onto bare $ZnIn_2S_4$, indicating that the specific surface area does not be responsible for the photocatalytic activity of these nanocomposites in this hybrid system.

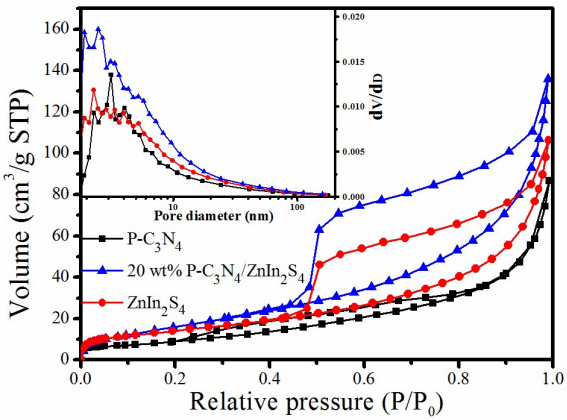

Fig.5 Nitrogen adsorption-desorption isotherms and the pore size distribution plots (inset) of pure P-C_3N_4, bare $ZnIn_2S_4$ and 20 wt% P-C_3N_4/$ZnIn_2S_4$ nanocomposites.

The photocatalytic activities of as-prepared samples were evaluated by photoredox reactions of 4-nitroaniline (4-NA) to corresponding 4-phenylenediamine (4-PDA) under visible light irradiation. Controllable experiments suggested that almost no appreciable 4-PDA produced in the absence of photocatalyst. Besides, the appropriate photocatalytic conditions were explored to achieve the conversion maximum by controlling reaction atmosphere and adding different active species capture agent. Fig. S4 displays the influence of catalytic condition on 4-NA conversion. Note that, the photocatalytic activity of 20 wt% P-C_3N_4/$ZnIn_2S_4$ photocatalyst presents remarkably suppression in the absence of either NH_4COOH or N_2 purge. While the $K_2S_2O_8$, served as electron scavenger, were added into the photoredox reaction, no conversion can be observed, indicating that photo-generated electron plays an essential role in driving the photocatalytic reduction of 4-NA. As a consequence, the hole scavenger and inert atmosphere are essential for high-efficient photo-reduction reaction. Therefore, the photocatalytic reduction reaction of 4-NA were performed with addition of ammonium formate as a hole quencher under N_2 atmosphere as shown in Fig.6. Fig. 6a shows the temporal concentration variation of 4-NA over 20 wt% P-C_3N_4/$ZnIn_2S_4$ nanocomposites at settled intervals, which were monitored by examining the maximal absorption in UV–vis spectra at 381.7 nm. Obviously, the intensity of characteristic absorption corresponding to 4-NA increases with irradiation time and two new peaks at 301.6 and 235.3 nm belonging to 4-PDA appeared and successively increased as the reaction proceeded, indicative of the successful transformation of nitro group to amine group. It is clearly seen that all photocatalysts exhibit the photocatalytic activities for the selective reduction of 4-NA solution under visible light irradiation and binary P-C_3N_4/$ZnIn_2S_4$ nanocomposites shows remarkably enhanced photocatalytic performance in comparison with pure P-C_3N_4 and pristine $ZnIn_2S_4$ (Fig. 6b). In particular, the 20 wt% P-C_3N_4/$ZnIn_2S_4$ sample possesses the best photocatalytic activity with the conversion up to 99.4% with the exposure of 90 min visible light irradiation. In contrast, only 38.7%, 67.9%, 88.0%, 79.3% and 19.4% of aromatic nitro compounds are transformed within 90 min over

$ZnIn_2S_4$, 5 wt% P-C_3N_4/$ZnIn_2S_4$, 10 wt% P-C_3N_4/$ZnIn_2S_4$, 30 wt% P-C_3N_4/$ZnIn_2S_4$ and P-C_3N_4, respectively. This can be attributed to high efficiency of charge separation induced by the intimate heterojunction interface built between $ZnIn_2S_4$ and P-C_3N_4. The light absorption is the premise of the generation of charge carrier pairs and the decreased light absorption in P-C_3N_4/$ZnIn_2S_4$ nanocomposites is extremely unfavorable to photocatalytic activity. However, the fast electron transfer via heterogeneous interface can effectively promote the efficient separation of hole and electron pairs, thus benefiting the photocatalytic activities of P-C_3N_4/$ZnIn_2S_4$ heterostructures. Also, the P-C_3N_4/$ZnIn_2S_4$ nanocomposites exhibits significant enhancement of photocatalytic activity towards MO degradation (Fig. S5). In addition, the photocatalytic conversion of P-C_3N_4 is superior to g-C_3N_4 (16.9 %) because of faster charge separation created by P doping into g-C_3N_4.[27]

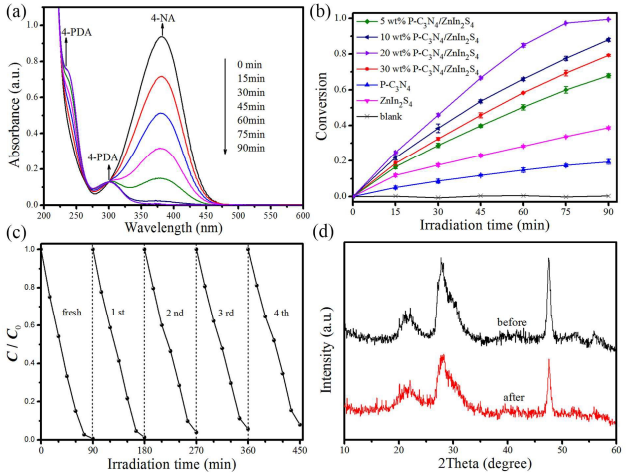

Fig.6 (a) UV-vis absorption spectra of 4-NA and 4-PDA; (b) Photocatalytic selective reduction of 4-NA to 4-PDA over pure P-C_3N_4, blank $ZnIn_2S_4$ and P-C_3N_4/$ZnIn_2S_4$ nanocomposites with the presence of ammonium formate and N_2 purge at room temperature (λ > 400 nm); (c) the reusability of the as-prepared 20 wt% P-C_3N_4/$ZnIn_2S_4$ nanocomposites for selective reduction of 4-NA; (d) XRD patterns before and after four consecutive photocatalytic reactions.

Not only the photocatalytic activity, but also the photo-stability is an important index for catalyst assessment. However, as we known, the pure sulfide would suffer greatly from photocorrosion during the photocatalytic process. Therefore, the modification for sulfide or sulfide based nanocomposites to achieve excellent stability is highly desired. To evaluate the photo-stability of as-prepared $ZnIn_2S_4$ based P-C_3N_4/$ZnIn_2S_4$ nanocomposites, the recycling photocatalytic reduction of 4-NA have been performed over 20 wt% P-C_3N_4/$ZnIn_2S_4$ nanocomposites under visible light irradiation. As displayed in Fig. 6c, no noticeable deterioration of photocatalytic performance is observed after four successive recycling runs, suggesting that the photocorrosion of $ZnIn_2S_4$ could be efficiently inhibited by coupling with P-C_3N_4 sheets. The outstanding stability of 20 wt% P-C_3N_4/$ZnIn_2S_4$ nanocomposites was further determined by analyzing the XRD patterns (Fig.6d). The result reveals that phase structure of 20 wt% P-C_3N_4/$ZnIn_2S_4$ retains intact after recycling reaction, indicating excellent photo-stability of P-C_3N_4/$ZnIn_2S_4$ nanocomposites. In this hybrid sample, the improved photo-stability can be attributed to the highly efficient separation of charge carrier pairs based on perfect interfacial contact between P-C_3N_4 nanosheets and $ZnIn_2S_4$ nanosheets.

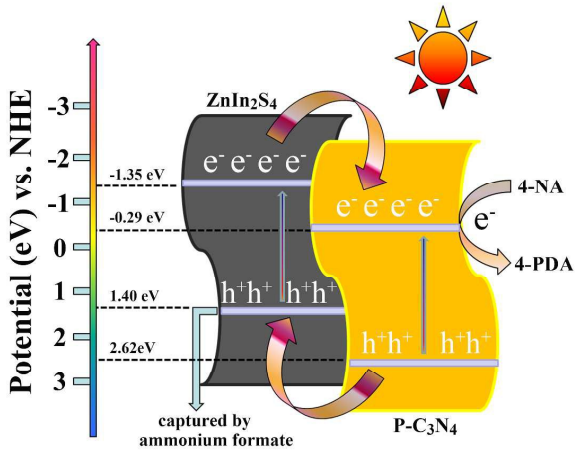

Fig. 7 Schematic illustration of photocatalytic reaction and charge transfer of the P-C_3N_4/$ZnIn_2S_4$ nanocomposites under visible light irradiation.

To explain the photocatalytic process of P-C_3N_4/$ZnIn_2S_4$ nanocomposites as visible light driven photocatalysts towards nitro-reduction, the transfer path of photo-generated charge carriers' pairs must be investigated. Therefore, the band edge potentials of $ZnIn_2S_4$ and P-C_3N_4 were estimated by the combination of Mulliken electronegativity theory and valence band X-ray photoelectron spectroscopy (VB-XPS). According to previous reports, the equation of Mulliken electronegativity theory can be described by[38,39]

$$E_{CB} = \chi - E_e - 0.5\,E_g$$

where E_{CB} is the conduction band edge potential, χ is the electronegativity of the semiconductor, expressed as the geometric mean of the absolute electronegativity of the constituent atoms, defined as the arithmetic mean of the first ionization energy and the atomic electron affinity. E_e represents the free electrons energy on the hydrogen scale ca. 4.5 eV. Eg is the band gap of the semiconductor. The χ value of $ZnIn_2S_4$ sample is 4.53 eV. As a consequence, the E_{VB} and E_{CB} values of $ZnIn_2S_4$ are calculated as 1.40 and -1.35 eV. Fig. S6 displays the VB-XPS spectra of $ZnIn_2S_4$ and P-C_3N_4, from which the valence band maximum (VBM) of these two samples were separately determined to be 1.22 eV and 2.42 eV, meaning the lower VBM potential (1.20 eV) of P-C_3N_4 than that of hexagonal $ZnIn_2S_4$. On the basis of above analyses, the calculated CB and VB edge potentials of P-C_3N_4 are decided at -0.29 eV and +2.62 eV, respectively. Obviously, the band-to-band transition of photo-induced holes and electrons can be motivated with exposure of visible light due to their narrow band gaps corresponding to visible light absorption. When irradiated by visible light, both $ZnIn_2S_4$ and P-C_3N_4 have ability to absorb the photon energy to be excited to generate holes and electrons, meanwhile the photo-generated electrons would transit to the CB from VB. Considering the band edge potentials of $ZnIn_2S_4$ are more positive than those of P-C_3N_4, based on the construction of close heterojunction interface

and well-matched band structure between $ZnIn_2S_4$ and P-C_3N_4, the excited electrons in the CB of $ZnIn_2S_4$ could directly to CB of P-C_3N_4. Holes would jump from VB of P-C_3N_4 to that of $ZnIn_2S_4$ simultaneously. Fig.7 shows the charge transfer path and photocatalytic reaction using P-C_3N_4/$ZnIn_2S_4$ nanocomposites. During such transfer process, the photo-generated holes and electrons pairs can be effectively separated, thus decreasing the recombination rate of charge carrier pairs. As a result, the transferred electrons would enrich in the VB of P-C_3N_4 to be electrons centre to react with nitro group and the holes leaving on the $ZnIn_2S_4$ would be consumed by adding the hole scavenger. The relevant transfer paths of charge carrier pairs during photo-reduction are given as follows:

$ZnIn_2S_4 + hv \rightarrow ZnIn_2S_4 (h^+ + e^-)$ (1)

P-C_3N_4 + $hv \rightarrow$ P-C_3N_4 ($h^+ + e^-$) (2)

$ZnIn_2S_4 (h^+ + e^-)$ + P-C_3N_4 ($h^+ + e^-$) $\rightarrow ZnIn_2S_4 (h^+)$ + P-C_3N_4 (e^-) (3)

$ZnIn_2S_4 (h^+)$ + $NH_4COOH \rightarrow ZnIn_2S_4 + NH_4COOH (h^+)$ (4)

P-C_3N_4 (e^-) + $-NO_2 + H^+ \rightarrow$ P-C_3N_4 + $-NH_2$ (5)

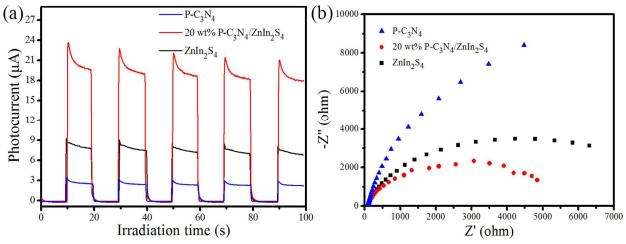

Fig. 8 (a) Transient photocurrent-time (I-t) curves and (b) electro-chemical impedance spectroscopy (EIS) Nyquist plots of different samples in 0.1 M Na_2SO_4 solution.

In principle, many factors, including phase structure, morphology, light absorption intensity, specific surface area and separation efficiency of photo-generated carrier charge pairs, etc. play important roles in deciding the photocatalytic activities. [40, 41] That is to say, the overall photocatalytic performance originates from the synergistic effects of all key factors above-concerned. However, the similar phase structure and morphology, the decrease light absorption and specific surface area indicate these factors are not responsible for the significant enhancement of photocatalytic reduction for 4-NA. In this binary system, the construction of heterogeneous interface may be a key point for high photocatalytic activity because the nanocomposites with well-matched band structure would benefit from photocatalysis owing to the faster separation of photoinduced charge carrier pairs via heterojunction, which serves as the channel for the transmission of photo-induced hole and electron pairs. Fig. 8 shows the photocurrent response of different samples with the exposure of discontinuous visible light. It can be clearly seen that bare $ZnIn_2S_4$ exhibits higher photocurrent than P-C_3N_4, but not as significant enhancement as 20 wt% P-C_3N_4/$ZnIn_2S_4$ nanocomposites, which implies that photoinduced charge carriers can be separated efficiently after coupling. The efficient charge transfer was further verified by the electrochemical impedance spectra (EIS) analysis as shown in Fig. 8b. The EIS Nyquist plots reveal that the prepared 20 wt% P-C_3N_4/$ZnIn_2S_4$ nanocomposite owns smaller semicircle in comparison with those of its counterparts, suggesting the hybridization among P-C_3N_4 and $ZnIn_2S_4$ can enhance the separation and transfer efficiency of charge carrier pairs.

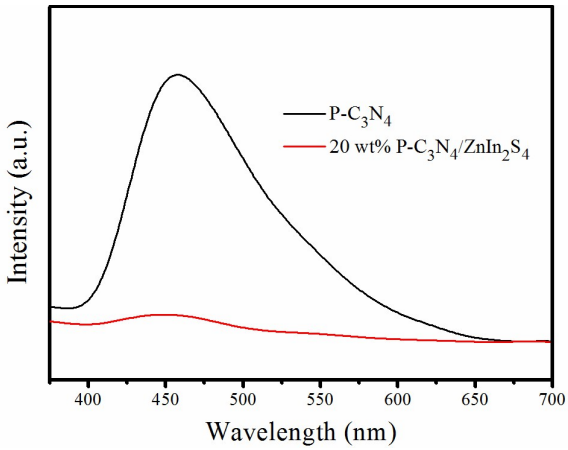

Fig. 9 Photoluminescence spectra of pure P-C_3N_4 and 20 wt% P-C_3N_4/$ZnIn_2S_4$ nanocomposite.

Furthermore, the photoluminescence (PL) spectra were employed to characterize the separation efficiency of photo-generated charger carriers since PL originates from the recombination of free charge carriers.[42] Usually, the PL intensity reflects the recombination rate between holes and electrons. The lower PL intensity, the faster separation of charge carriers pairs. As shown in Fig. 9, the 20 wt% P-C_3N_4/$ZnIn_2S_4$ nanocomposites displays the lower intensity, which is well agreement with photocurrent response and EIS spectra.

4. Conclusions

In summary, we firstly design and fabricate a series of P-C_3N_4/$ZnIn_2S_4$ heterostructured photocatalysts via regulation of mass ratio between P-C_3N_4 and $ZnIn_2S_4$ at mixed solvent system. The photocatalytic reduction of 4-NA in liquid phase was used to evaluate the catalytic activity of P-C_3N_4/$ZnIn_2S_4$ nanocomposites under visible light irradiation. The results reveal that P-C_3N_4/$ZnIn_2S_4$ nanocomposites present an excellent visible light photocatalytic activity for the reduction nitro group, especially 20 wt% P-C_3N_4/$ZnIn_2S_4$. Besides, the 20 wt% P-C_3N_4/$ZnIn_2S_4$ exhibits high stability during the recycling photocatalytic reaction. The enhancement of visible light photocatalytic activity resulted from the high separation efficiency of photoinduced electron-hole pairs on the basis of the construction of close heterogeneous interface, which were confirmed by sufficient evidences. We hope this work could provide new insights into the application of g-C_3N_4 based nanocomposites and strengthen the stability of sulfide based compounds.

Acknowledgements

The financial supports from National Natural Science Foundation of China (Grant no. 51272107 and Grant no. 51572126) are gratefully acknowledged. This investigation is also supported by the Priority Academic Program

Development (PAPD) of Jiangsu Higher Education Institutions and the Fundamental Research Funds for the Central Universities (Grant no. 30920140132038).

Notes and references

1 J. Zhang, Q. Wang, L. Wang, X. Li and W. Huang, *Nanoscale*, 2015, **7**,10391-10 397.
2 J. Zhang, L. Wang, X. Liu, X. Li and W. Huang, *J. Mater. Chem. A*, 2015, **3**, 535-541.
3 L. Li, Y. Yu, G.J. Ye, Q. Ge, X. Ou, H. Wu, D. Feng, X.H. Chen and Y. Zhang, *Nature Nanotech.*, 2014, **9**, 372-377.
4 H. Liu, A.T. Neal, Z. Zhu, Z. Luo, X. Xu, D. Tománek and P.D. Ye, *ACS Nano*, 2014, **8**, 4033-4041.
5 X. Zhang, X. Xie, H. Wang, J. Zhang, B. Pan and Y. Xie, *J. Am. Chem. Soc.*, 2013, **135**, 18-21.
6 A. Fujishima and K. Honda, *Nature*, 1972, **238**, 37–39.
7 Q. Li, C. Cui, H. Meng and J. Yu, *Chem. Asian J.*, 2014, **9**, 1766-1770.
8 N.S. Chaudhari, S.S. Warule and B.B. Kale, *RSC Adv.*, 2014, **4**, 12182-12187.
9 J. Zhou, G. Tian, Y. Chen, X. Meng, Y. Shi, X. Cao, K. Pan and H. Fu, *Chem. Commun.*, 2013, **49**, 2237-2239.
10 B. Gao, L. Liu, J. Liu and F. Yang, *Appl. Catal. B: Environ.*, 2014, **147**, 929-939.
11 X. Wang, K. Maeda, X. Chen, K. Takanabe, K. Domen, Y. Hou, X. Fu and M. Antonietti, *J. Am. Chem. Soc.*, 2009, **131**, 1680-1681.
12 Q. Lin, L. Li, S. Liang, M. Liu, J. Bi and L. Wu, *Appl. Catal. B: Environ.*, 2015, **163**, 135-142.
13 D. Zheng, C. Huang and X. Wang, Nanoscale, 2015, 7, 465-470.
14 X. Bai, L. Wang, R. Zong and Y. Zhu, J. Phys. Chem. C, 2013, 117, 9952-9961.
15 H. Nie, M. Ou, Q. Zhong, S. Zhang and L. Yu, *J. Hazard. Mater.*,2015, **300**, 598-606.
16 Y. Li, H. Xu, S. Ouyang, D. Lu, X. Wang, D. Wang and J. Ye, *J. Mater. Chem. A*, 2016, DOI: 10.1039/c5ta05128b.
17 W. Zhao, Y. Guo, S. Wang, H. He, C. Sun and S. Yang, *Appl. Catal. B: Environ.*, 2015, **156**, 335-343.
18 W. Chen, T.Y. Liu, T. Huang, X.H. Liu, J.W. Zhu, G.R. Duan and X. J. Yang, *J Mater Sci*, 2015,**50**, 8142-8152.
19 G. Liu, P. Niu, C. Sun, S.C. Smith, Z. Chen, G. Q. Max Lu and H.M. Chen, *J. Am. Chem. Soc.*, 2010, **132**, 11642-11648.
20 P. Niu, L.C. Yin, Y.Q. Yang, G. Liu and H.M. Chen, *Adv. Mater.*, 2014, **26**, 8046-8052.
21 J. Li, B. Shen, Z. Hong, B. Lin, B. Gao and Y. Chen, *Chem. Commun.*, 2012, **48**, 12017-12019.
22 F. He, G. Chen, Y. Zhou, Y. Yu, Y. Zheng and S. Hao, *Chem. Commun.*, 2015, **51**, 16244-16266.
23 W. Chen, T.Y. Liu, T. Huang, X.H. Liu, J.W. Zhu, G.R. Duan and X.J. Yang, *Appl. Surf. Sci.*, 2015, **355**, 379-387.
24 F. Cheng, H. Wang and X. Dong, *Chem. Commun.*, 2015, **51**, 7176-7179.
25 Z.F. Huang, J. Song, L. Pan, Z. Wang, X. Zhang, J.J. Zou, W. Mi, X. Zhang and L. Wang, *Nano Energy*, 2015, **12**, 646-656.
26 Y.P. Zhu, T.Z. Ren and Z.Y. Yuan, *ACS Appl. Mater. Interfaces*, 2015, **7**, 16850-16856.
27 Y. Zhou, L. Zhang, J. Liu, X. Fan, B. Wang, M. Wang, W. Ren, J. Wang , M. Li and J. Shi, *J. Mater. Chem. A*, 2015, **3**, 3862-38 67.
28 W. Chen, G.R. Duan, T.Y. Liu, S.M. Chen and X.H. Liu, *Mat. Sci. Semicond. Process.*, 2015, **35**, 45-54.
29 J. Sun, Y. Fu, G. He, X. Sun and X. Wang, *Appl. Catal. B: Environ.*, 2015, **165**, 661-667.
30 C. Tan, G. Zhu, M. Hojamberdiev, K.S. Lokesh, X. Luo, L. Jin, J. Zhou and P. Liu, *J. Hazard. Mater.*, 2014, **278**, 572-583.
31 W. Chen, Z. Chen, T. Liu, Z. Jia and X. Liu, *J. Environ. Chem. Eng.*, 2014, **2**, 1889-1897.
32 S. Martha, A. Nashim and K.M. Parida, *J. Mater. Chem. A*, 2013, **1**, 7816-7824.
33 K. Li, L. Yan, Z. Zeng, S. Luo, X. Luo, X. Liu, H. Guo and Y. Guo, *Appl. Catal. B: Environ.*, 2014, **156-157**, 141-152.
34 K. Li, Z. Zeng, L. Yan, S. Luo, X. Luo, M. Huo and Y. Guo, *Appl. Catal. B: Environ.*, 2015, **165**, 428-437.
35 L. Ye, J. Fu, Z. Xu, R. Yuan and Z. Li, *ACS Appl. Mater. Interfaces*, 2014, **6**, 3483-3490.
36 K.S.W. King, D.H. Everett, R.A.W. Haul, L. Moscou, R.A. Pierotti, J. Rouquerol and T. Siemieniewska, *Pure Appl. Chem.*, 1985, **57**, 603-619.
37 B. Gao, L. Liu, J. Liu and F. Yang, *Appl. Catal. B: Environ.*, 2013, **129**, 89-97.
38 C. Xing, Y. Zhang, W. Yan and L. Guo, *Int J Hydrogen Energy*, 2006, **31**, 2018-2024.
39 J. Zhang, J. Yu, Y. Zhang, Q. Li and J.R. Gong, *Nano Lett.*, 2011, **11**, 4774–4779.
40 X. Bai, L. Wang and Y. Zhu, *ACS Catal.*, 2012, **2**, 2769-2778.
41 N. Zhang, S. Liu, X. Fu and Y.J. Xu, *J. Phys. Chem. C*, 2011, **115**, 9136-9145.
42 W. Chen, T.Y. Liu, T. Huang, X.H. Liu, G.R. Duan, X.J. Yang and S.M. Chen, *RSC Adv.*, 2015, **5**, 101214-101220.
43 Y. Li, L. Fang, R. Jin, Y. Yang, X. Fang, Y. Xing and S. Song, *Nanoscale*, 2015, **7**,758-764.